

Friend or Foe? Harnessing Controllable Overfitting for Anomaly Detection

Long Qian^{1,2} Bingke Zhu^{1,3} Yingying Chen^{1,3} Ming Tang^{1,2} Jinqiao Wang^{1,2,3}

¹ Foundation Model Research Center, Institute of Automation,
Chinese Academy of Sciences, Beijing, China

² School of Artificial Intelligence, University of Chinese Academy of Sciences, Beijing, China

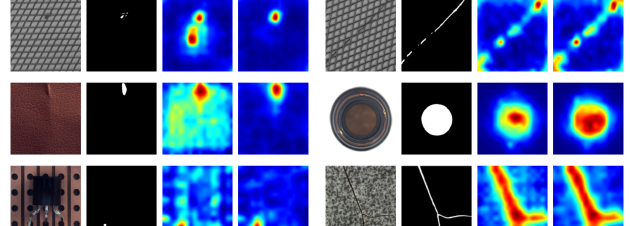
³ Objecteye Inc., Beijing, China

qianlong2024@ia.ac.cn

{bingke.zhu,yingying.chen,tangm,jqwang}@nlpr.ia.ac.cn

Abstract

Overfitting has long been stigmatized as detrimental to model performance, especially in the context of anomaly detection. Our work challenges this conventional view by introducing a paradigm shift—recasting overfitting as a controllable and strategic mechanism for enhancing model discrimination capabilities. In this paper, we present Controllable Overfitting-based Anomaly Detection (COAD), a novel framework designed to leverage overfitting for optimized anomaly detection. We propose the Aberrance Retention Quotient (ARQ), a novel metric that systematically quantifies the extent of overfitting, enabling the identification of an optimal "golden overfitting interval" $ARQ_{optimal}$. Within this interval, overfitting is leveraged to significantly amplify the model's sensitivity to anomalous patterns, while preserving generalization to normal samples. Additionally, we present the Relative Anomaly Distribution Index (RADI), an innovative metric designed to complement AUROC-pixel by providing a more versatile and theoretically robust framework for assessing model performance. RADI leverages ARQ to track and evaluate how overfitting impacts anomaly detection, offering an integrated approach to understanding the relationship between overfitting dynamics and model efficacy. Our theoretical work also rigorously validates the use of Gaussian noise in pseudo-anomaly synthesis, providing the foundation for its broader applicability across diverse domains. Empirical evaluations demonstrate that our controllable overfitting method not only achieves State-Of-The-Art(SOTA) performance in both one-class and multi-class anomaly detection tasks but also redefines overfitting from a modeling challenge into a powerful tool for optimizing anomaly detection.



(a) False Positive Cases (b) False Negative Cases

Figure 1. Each subfigure presents a sequence from left to right, displaying: the original image, the ground truth, the results from other methods, like *RD* [6], *RD++* [23], *UniAD* [28] and *DiAD* [11], and our results after overfitting enhancement based on existing frameworks with *COAD*. (a) illustrates a significant reduction in the false positive rate after applying our overfitting approach. (b) highlights the reduction in the false negative rate, demonstrating enhanced sensitivity towards true anomalies with our method. The consistent improvement across both metrics indicates the effectiveness of our methods in refining detection accuracy.

1. Introduction

In the traditional context of machine learning, overfitting has long been perceived as an undesirable phenomenon, just like [3, 8, 10, 20], traditionally viewed as the result of a model excessively memorizing training data, leading to compromised generalization capabilities. However, we challenge this conventional wisdom by extending the concept beyond the domain of anomaly detection, positioning controllable overfitting as a versatile mechanism for enhancing model sensitivity across a wide range of applications. This leads us to the central question that underpins our work: can overfitting be a friend rather than a foe in the domain of anomaly detection?

The conventional understanding of overfitting necessi-

tates a significant paradigm shift. Historically stigmatized as inherently detrimental to machine learning models, overfitting, as our research demonstrates, can under specific controlled conditions be repurposed as a powerful mechanism for enhancing model performance. In scenarios where training data consists solely of normal samples, we show that allowing the model to comprehensively memorize these features enhances its sensitivity to deviations—namely, anomalies—during testing. This reframing positions overfitting not as an inherent flaw to be avoided, but as a strategic asset to be leveraged effectively.

Anomaly detection in visual domains is a crucial task that aims to identify patterns that do not conform to expected behavior. Traditionally, anomaly detection relies on the notion of learning the distribution of normal data and distinguishing anomalies by identifying outliers. Various methods have been proposed to achieve this, including reconstruction-based approaches [15, 30, 31], embedding-based models [9, 13, 25, 32], and anomaly synthesis technique [4, 17, 23, 28].

We advance the notion of controllable overfitting, suggesting that a calculated and moderate degree of overfitting enables the model to capture intricate and subtle characteristics of the data. This heightened focus allows for a pronounced contrast when confronted with previously unseen deviations—precisely what is required for successful detection tasks, as opposed to a simplistic pursuit of generalization. This approach provides an opportunity to redefine how we evaluate model capabilities in environments devoid of training data that represents the full spectrum of possible scenarios. In this paper, we present *Controllable Overfitting-based Anomaly Detection*, called **COAD**.

Our theoretical framework and empirical validation jointly support this proposition. We demonstrate that, as the degree of overfitting increases, the score distribution for normal samples evolves accordingly, while the score distribution for anomalous samples remains stable. By introducing the *Aberrance Retention Quotient*, called **ARQ**, as an overfitting parameter, coupled with a noise loss term to finely control the degree of overfitting, we have identified an optimal "Golden Overfitting Interval" $ARQ_{optimal}$ that maximizes detection efficacy without compromising model reliability. This strategic balance enables robust differentiation between normal and anomalous samples, providing a substantial performance boost.

We also introduce a novel metric, the Relative Anomaly Distribution Index, called **RADI**, to differentiate from traditional *AUROC-pixel* measures. Unlike *AUROC-pixel*, **RADI** is derived from the cumulative distribution function (CDF) of the normal and anomalous pixel prediction score distributions. While **RADI** provides an indirect reflection of detection performance and maintains a similar trend to *AUROC-pixel*, it also offers a more versatile framework for theo-

cal modeling and practical discussion of model capabilities. This distinction underscores its value as a complementary tool, adding a new layer of analytical depth to our approach.

Moreover, we substantiate the rationale for employing Gaussian noise in pseudo-anomaly detection modules. Through calculating the Total Variation Distance (TVD) between actual anomaly data and a Gaussian distribution across the entire dataset, we obtain a fair result. This outcome indicates a high level of similarity between true anomalies and a Gaussian distribution, thereby providing a theoretical validation for the common practice of using Gaussian noise as an effective pseudo-anomaly generator in previous works like *GLASS* [4] and *SimpleNet* [17]. This insight not only strengthens our methodology but also offers a theoretical foundation for broader applications in anomaly detection frameworks.

To summarize, the key contributions of our work are as follows:

- We challenge and transcend the conventional understanding of overfitting, positioning it as a controllable and transformative mechanism capable of unlocking model capabilities beyond traditional boundaries.
- We introduce the **ARQ** to precisely regulate the overfitting degree and the **RADI** as a complementary metric to *AUROC-pixel*, providing a more adaptable tool for mathematical modeling and facilitating *Dual Control Mechanism* with the use of **COAD**.
- Our approach dismantles the demonization of overfitting, repurposing it as a generalizable module and achieving SOTA results in both *one-class* and *multi-class* anomaly detection tasks. We also provide a theoretical foundation for utilizing *Gaussian noise* as a preliminarily pseudo-anomaly generator.

2. Related Work

2.1. Overview of Anomaly Detection

Reconstruction-Based Method Reconstruction-based methods are founded on the hypothesis that models trained exclusively on normal data can successfully reconstruct normal instances while failing to do so for anomalies, thereby using reconstruction error as a measure of abnormality. Notable reconstruction-based approaches include Autoencoders (AE)[29, 33], Generative Adversarial Networks (GANs)[7, 15], and Reverse Distillation (RD)[6, 23]. Specific methods under these categories, such as *DSR*[31], *RealNet*[32], and *DRAEM*[30], attempt to learn the representation of normal data and generate accurate reconstructions for normal samples but tend to produce significant residuals for anomalous inputs.

Embedding-Based Method Recent developments have seen the use of embedding-based methods, besides

reconstruction-based methods. These models leverage pre-trained networks to extract features from input images, aiming to separate anomalies from normal samples within the feature space. Anomalies are identified based on the distance between their embeddings and those of normal samples. Techniques such as *Double-MMD RGP*[25], *RealNet*[32], *PyramidFlow*[13], and *CFlowAD*[9] utilize this paradigm, some of which employ a memory bank to store representative features and apply distance metrics to detect anomalies. Embedding-based methods are particularly valuable in high-dimensional feature spaces, where the intricate relationships between different regions of the data can be better captured using a pre-trained model’s learned representations.

Synthetic Anomaly Generation Another line of research focuses on synthetic anomaly generation, a strategy that involves creating pseudo-anomalies to augment training data and improve detection performance. These synthetic anomalies are used to provide explicit anomaly labels in the training set, converting the unsupervised task into a form of supervised learning. Notable techniques include *Cut-Paste* [14], which pastes cut-out normal patches in different positions, and methods such as *GLASS*[4], *UniAD*[28], *SimpleNet*[17], *RealNet*[32], and *DDPM* [12], all of which employ Gaussian noise to generate synthetic anomalies at both feature and image levels. These approaches help in training the model to differentiate between normal and abnormal samples, thus improving its ability to detect true anomalies. By contrast, methods such as *DRAEM*[30] and *DMDD* [16] employ Berlin noise or other forms of noise, which have not demonstrated the same level of effectiveness in anomaly detection tasks. In subsequent sections, we will theoretically justify the use of Gaussian noise in these pseudo-anomaly generation modules, establishing its effectiveness and reasonableness as an anomaly synthesis strategy.

2.2. One-class vs. Multi-class

Our method builds on existing frameworks in anomaly detection and requires a deep understanding of these foundational models. Without a comprehensive grasp of their structure and mechanisms, our method may be misapplied, leading to suboptimal outcomes. Hence, we will conduct demonstrative experiments from both *one-class* and *multi-class* perspectives.

One-class Anomaly Detection *One-class* anomaly detection focuses on modeling the distribution of normal data to identify deviations. Methods such as *RD* [6] and *RD++* [23] are foundational in this area. *RD* employs a pretrain model for feature extraction, while *RD++* further enhances this process for improved robustness.

Multi-class Anomaly Detection *Multi-class* anomaly detection handles diverse object categories and intra-class variations. Notable approaches like *UniAD* [28] and *HVQ-Trans* [18] effectively generalize across multiple classes.

2.3. Non-Diffusion vs. Diffusion-Based

For the purpose of making our method easier for readers to understand and apply, we have also supplemented it with the diffusion-based framework.

Non-diffusion methods Non-diffusion methods, such as *UniAD* [28], have been effective for anomaly detection but often face limitations in preserving the semantic consistency of anomalous regions, especially in complex settings.

Diffusion-based methods Diffusion-based methods have recently gained traction due to their exceptional reconstruction capabilities, as evidenced by *DiAD* [11], which stands out among contemporary methods. *DiAD* employs a diffusion framework for generating anomalies while maintaining semantic information.

3. Method

3.1. Overview

As Fig. 2 shows, our works provides an overview of our proposed framework for enhancing anomaly detection through controllable overfitting. We introduce *Controllable Overfitting-based Anomaly Detection*, called **COAD**. We systematically integrate novel elements such as *ARQ* for quantifying overfitting and *RADI* as a complementary metric for AUROC-pixel. These components collectively facilitate the monitoring, control, and optimization of the overfitting process to maximize model sensitivity while preserving generalization capabilities.

3.2. Quantifying Overfitting with Aberrance Retention Quotient

The exploration of overfitting has largely been confined to its avoidance, and there has been a conspicuous lack of systematic studies on how to control or even beneficially leverage overfitting for enhancing model capabilities. Moreover, existing research lacks a quantitative metric that accurately reflects the extent of overfitting, which is critical for understanding its implications and finding the “sweet spot” in model training. To fill this gap, we introduce the *Aberrance Retention Quotient*, called **ARQ**, a novel metric designed to quantify the degree of overfitting by capturing the model’s divergence from true data representation during training.

The *ARQ* is formally defined as follows:

$$ARQ = \frac{\sum_{i=1}^N (\hat{y}_i - y_i)}{\sum_{i=1}^N y_i}, \quad (1)$$

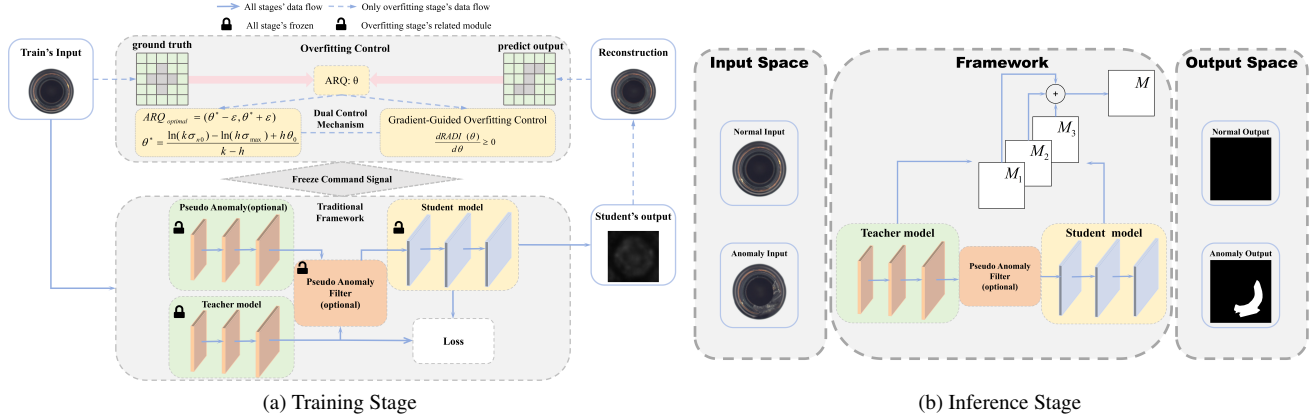


Figure 2. Comprehensive Framework for *COAD*. (a) Training Stage: In the traditional framework, the teacher model remains frozen throughout. The pseudo-anomaly generation and filtering components are optional, remaining unfrozen during the normal training stage but frozen during the controllable overfitting stage, under the guidance of the *Dual Control Mechanism*. The student model also remains unfrozen during normal training stage, with selective freezing employed during the controllable overfitting stages. When the *Dual Control Mechanism* fails, *Freeze Command Signals* are triggered, prompting the selective freezing of certain network layers in the traditional framework to effectively manage overfitting. (b) Inference Stage: The inference pipeline follows a similar procedure to the traditional framework, ensuring that the enhancements provided by *COAD* integrate seamlessly.

where N represents the total number of instances, \hat{y}_i represents the predicted output at the i^{th} instance, and y_i denotes the corresponding original ground truth value. The numerator captures the aggregate prediction deviation from the true labels across all data points, while the denominator represents the totality of the predicted target values, normalizing the aberrance in the context of the entire dataset.

ARQ is a core metric in our framework that quantifies the progression of overfitting during model training. By tracking ARQ , we identify the *golden overfitting interval*, where the model's sensitivity to anomalous patterns is maximized without compromising generalization. Specifically, we denote the interval of optimal ARQ as:

$$ARQ_{\text{optimal}} = [\theta - \delta, \theta + \delta], \quad (2)$$

where θ is the baseline value around which the optimal range is established, δ is a quantity of the same order of magnitude as θ , representing the permissible deviation from the baseline θ within the optimal range, which indicates the region in which the overfitting is leveraged most effectively.

As overfitting progresses, ARQ_{optimal} helps us mitigate false positives while reducing false negatives, Fig. 1a and Fig. 1b illustrate some cases. By effectively using ARQ , we transform overfitting into a controlled mechanism that enhances model robustness and discriminative power for anomaly detection.

3.3. Bridging Theoretical Modeling and Practical Anomaly Detection with *Relative Anomaly Distribution Index*

3.3.1 Probability Distribution Models of Normal and Anomalous Pixel Scores

To facilitate the mathematical treatment later, we made the following two assumptions, which were verified in subsequent experiments, please see Sec. 4.

Distribution of Normal Pixel Prediction Scores At an *Aberrance Retention Quotient* of $ARQ = \theta$, the prediction scores of normal pixels S_n follow a normal distribution dependent on θ :

$$S_n \sim N(\mu_n(\theta), \sigma_n(\theta)^2), \quad (3)$$

where the mean $\mu_n(\theta)$ and variance $\sigma_n(\theta)^2$ vary with ARQ . As the ARQ increases, the model's memory of normal samples is enhanced, potentially resulting in:

- The mean $\mu_n(\theta)$ becoming closer to the average value of the training data.
- The variance $\sigma_n(\theta)^2$ decreasing due to the model's predictions on normal samples becoming more stable.

The variance of normal pixel prediction scores decreases exponentially with increasing ARQ , expressed as:

$$\sigma_n(\theta) = \sigma_{n0} e^{-k\theta}, \quad (4)$$

where σ_{n0} is the initial variance (without overfitting), and k is a positive constant representing the rate at which variance

decreases. This relationship shows that as the model overfits, its prediction on normal samples becomes more stable.

Distribution of Anomalous Pixel Prediction Scores The prediction scores of anomalous pixels S_a follow a fixed normal distribution that does not change with ARQ :

$$S_a \sim N(\mu_a, \sigma_a^2), \quad (5)$$

since anomalous pixels are not present during training, and the model cannot memorize them.

3.3.2 Introduction of $RADI$

After these assumptions, we introduce the ***Relative Anomaly Distribution Index***, called ***RADI***, a novel metric designed to bridge theoretical modeling and practical anomaly detection. Unlike traditional metrics such as ***AUROC***, which are often used to evaluate model performance in anomaly detection tasks, ***RADI*** provides an indirect yet insightful measure of the model’s capacity to differentiate between normal and anomalous samples. This makes it particularly valuable for theoretical analyses, while also retaining practical utility in assessing model effectiveness.

The ***RADI*** quantifies the overlap between normal and anomalous score distributions, akin to the *Wilcoxon rank-sum* [24] and *Mann-Whitney U tests* [19]. ***RADI*** is calculated using the cumulative distribution function (CDF) of the score distributions:

$$\begin{aligned} RADI(ARQ) &= P(S_a > S_n) \\ &= \int_{-\infty}^{\infty} P(S_a > x) f_{S_n}(x) dx, \end{aligned} \quad (6)$$

where S_a and S_n represent the scores of anomalous and normal pixels, respectively.

It might seem counterintuitive why using ***RADI*** as an indicator would enhance model performance, as one might think that maximizing this value would lead to the model predicting everything as anomalous. However, ***RADI*** itself is not directly used for model optimization; rather, it serves as a metric to reflect the optimization outcome and help identify the extent to which normal and anomalous distributions are distinguishable. The goal is to ensure that anomalies receive consistently higher scores compared to normal samples, which allows the model to achieve better discrimination.

Moreover, the relationship between overfitting and variance is controlled by Eq. (8), which ensures that the variance of normal pixel predictions ($\sigma_n(\theta)$) does not decrease to zero due to the noise term $\sigma_{\text{noise}}(\theta)$. This prevents the variance from collapsing entirely, maintaining a distinction

between normal and anomalous scores. Thus, ***RADI*** can increase without the model predicting all samples as anomalous, as variability in normal predictions remains above a non-zero threshold, sustaining a balance between sensitivity to anomalies and generalization.

RADI provides a probabilistic assessment of whether anomalous scores exceed normal scores, offering insights into model discrimination. While similar to ***AUROC*** in reflecting a model’s ability to distinguish between normal and anomalous samples, ***RADI*** calculates this directly through distribution comparison rather than at multiple thresholds. It is particularly useful for quick theoretical assessments, whereas ***AUROC*** is better suited for comprehensive performance evaluations across thresholds.

Overall, ***RADI*** complements ***AUROC*** by providing a simplified measure of the model’s discriminative power, effectively reflecting its trend without requiring threshold-based evaluations.

3.3.3 Theoretical Derivation of Optimal Overfitting Conditions

For our case, where both S_a and S_n follow normal distributions, ***RADI*** can be further expressed in a simplified analytical form:

$$RADI(\theta) = \Phi \left(\frac{\mu_a - \mu_n}{\sqrt{\sigma_n(\theta)^2 + \sigma_a^2}} \right), \quad (7)$$

where Φ is the *CDF* of the standard normal distribution. In this case, μ_a and μ_n are the means of the anomaly and normal pixel score distributions, respectively, while σ_a and $\sigma_n(\theta)$ are their respective standard deviations, with θ representing the *Aberrance Retention Quotient*.

Eq. (7) highlights the dependence of ***RADI*** on the statistical properties of the score distributions. As θ increases, the standard deviation $\sigma_n(\theta)$ of the normal scores will decrease due to the model’s increasing ability to memorize normal patterns, which results in a more stable distribution for normal scores. This reduction in variance directly affects the value of ***RADI***, increasing the probability that the anomalous scores are distinguished from normal scores, thereby enhancing the detection capability of the model.

However, when overfitting is excessive, the model may start to memorize noise, leading to instability in prediction scores, and the variance $\sigma_n(\theta)$ will no longer decrease and could even increase. To describe this phenomenon, we introduce a noise term:

$$\sigma_n(\theta) = \sigma_{n0} e^{-k\theta} + \sigma_{\text{noise}}(\theta), \quad (8)$$

where $\sigma_{\text{noise}}(\theta)$ represents the noise impact induced by overfitting and can be expressed as:

$$\sigma_{\text{noise}}(\theta) = \sigma_{\text{max}}(1 - e^{-h(\theta - \theta_0)}), \quad \text{for } \theta > \theta_0, \quad (9)$$

where σ_{max} is the maximum noise variance, h controls the rate of increase of noise variance, and θ_0 is the threshold of ARQ where noise starts to appear. When $\theta \leq \theta_0$, $\sigma_{\text{noise}}(\theta) = 0$.

To find the optimal *Aberrance Retention Quotient* of $ARQ = \theta^*$ that maximizes $RADI$, we calculate the derivative of $\text{AUROC}_{\text{pixel}}(\theta)$ and set it to zero.

The derivative is as below and we set the derivative to zero:

$$\frac{dRADI(\theta)}{d\theta} = \phi(z(\theta)) \cdot \frac{dz(\theta)}{d\theta} = 0, \quad (10)$$

where $\phi(z)$ is the probability density function of the standard normal distribution.

$$\frac{dz(\theta)}{d\theta} = -\frac{(\mu_a - \mu_n) \cdot \sigma_n(\theta) \cdot \frac{d\sigma_n(\theta)}{d\theta}}{(\sigma_n(\theta)^2 + \sigma_a^2)^{3/2}} = 0, \quad (11)$$

This implies either $\sigma_n(\theta) = 0$ (unrealistic as variance cannot be zero) or $\frac{d\sigma_n(\theta)}{d\theta} = 0$. Thus, solving yields:

$$\theta^* = \frac{\ln(k\sigma_{n0}) - \ln(h\sigma_{\text{max}}) + h\theta_0}{k - h}. \quad (12)$$

3.3.4 Dual Control Mechanism and Freeze Command Signals

We define *Aberrance Retention Quotient* of $ARQ = \theta$, adjusted to optimize the *pixel-level AUROC*. The mathematical relationship between ARQ and $AUROC$ is established by monitoring the gradient. We call it *Gradient-Guided Overfitting Control*.

$$\frac{dRADI(\theta)}{d\theta} \geq 0. \quad (13)$$

We integrate ARQ_{optimal} in Eq. (2) and *Gradient-Guided Overfitting Control* in Eq. (13) and call this combined control mechanism the *Dual Control Mechanism*:

$$\frac{dRADI(\theta)}{d\theta} \geq 0, \quad \text{for } \theta \in ARQ_{\text{optimal}}. \quad (14)$$

If *Dual Control Mechanism* fails, the *Dual Control Mechanism* triggers *Freeze Command Signals*, which prompt whether freeze certain network layers, beginning with lower-level feature extraction layers and moving upwards.

The rationale for progressively freezing certain layers while overfitting the other parts lies in the architecture's functional partitioning. Lower layers are responsible for extracting fundamental features, which are common across both normal and anomalous data. Freezing these layers

early preserves their ability to extract generalizable features, preventing degradation due to overfitting. Conversely, keeping deeper layers unfrozen during the overfitting stage enables the model to specialize in identifying unique, high-level features that are more discriminative between normal and anomalous samples. This approach helps maintain generalization while enhancing sensitivity to rare patterns, ultimately boosting anomaly detection performance without succumbing to the pitfalls of overfitting the entire model.

4. Experiments

4.1. Dataset

We evaluate our method using the MVTec AD dataset [1], which is a comprehensive, real-world dataset for unsupervised anomaly detection tasks. The MVTec AD dataset includes 15 categories, comprising 3629 images for training and 1725 images for testing. The dataset provides pixel-level annotations for each anomaly, making it suitable for evaluating both image-level classification and pixel-level segmentation tasks.

4.2. Comparison with SOTAs

In this section, we compare the performance of our proposed method with several SOTA anomaly detection methods in both one-class and multi-class tasks.

Using the optimal ARQ value θ derived from the ARQ_{optimal} as indicated by Eq. (12), we set ARQ to 0.006 for *one-class* tasks and 0.06 for *multi-class* tasks. ARQ_{optimal} is defined as $\theta \in [0.001, 0.011]$ for *one-class* tasks and $\theta \in [0.01, 0.11]$ for *multi-class* tasks, where the balance between overfitting and generalization is optimal for anomaly detection. We saved model states within these intervals and evaluated their performance across respective benchmarks to ensure robust detection.

Furthermore, during model training, we adopted a *Dual Control Mechanism* for Optimal Detection Performance approach in our framework *COAD*, as detailed in Eq. (14), and when *Dual Control Mechanism* fails, it triggers *Freeze Command Signals*, prompting the selective freezing of certain network layers in the traditional framework.

Our method builds upon existing anomaly detection frameworks. Initially, we perform standard training on the original model. Following this, we transition into the controllable overfitting stage, during which the model is further trained using our *COAD* framework. This stage utilizes *Dual Control Mechanism* in Eq. (14). All pseudo-anomaly generation in this stage is performed using Gaussian noise to introduce controlled variability, which aids in refining the model's sensitivity to anomalies. Additionally, the learning rate is reduced to $\frac{1}{10}$ of that used in the normal training stage, allowing the model to make finer adjustments.

After training, the inference of the model proceeds in

Category	DSR [31]	PatchCore [21]	BGAD [26]	SimpleNet [17]	GLASS [4]	RD [6]	RD (+COAD)	RD++ [23]	RD++ (+COAD)
Object	Bottle	99.6/98.8	100/98.5	100/98.9	100/98.0	100/99.3	100/98.7	100/98.8	100/99.6
	Cable	95.3/97.7	99.8/98.4	97.9/98.0	100/97.5	99.8/98.7	95.0/97.3	97.9/97.7	99.3/98.4
	Capsule	98.3/91.0	98.1/99.0	97.3/98.0	97.8/98.9	99.9/99.4	96.3/98.3	98.8/98.4	99.0/98.8
	Hazelnut	97.7/99.1	100/98.7	99.3/98.5	99.8/98.1	100/99.4	99.9/98.9	100/99.1	100/99.2
	Metal Nut	99.1/94.1	100/98.3	99.3/97.7	100/98.8	100/99.4	100/97.3	100/97.7	100/98.1
	Pill	98.9/94.2	96.4/97.8	98.8/98.0	98.6/98.6	99.3/99.4	96.6/98.2	97.9/98.4	98.4/98.3
	Screw	95.9/98.1	98.4/99.5	92.3/99.2	98.7/99.2	100/98.5	97.0/99.5	99.5/99.6	98.9/ 99.7
	Toothbrush	100/99.5	100/98.6	86.9/98.7	100/98.5	100/99.3	99.5/98.9	100/99.1	100/99.4
	Transistor	96.3/80.3	99.9/96.1	99.7/93.9	100/97.0	99.9/97.6	96.7/92.4	98.9/93.4	98.5/94.3
	Zipper	98.5/98.4	99.4/98.9	97.8/98.7	99.9/98.9	100/99.6	98.5/98.2	99.1/98.7	98.6/98.8
Texture	Carpet	99.6/96.0	98.6/99.1	99.8/99.4	99.7/98.4	99.8/99.6	98.9/98.9	99.8/99.2	99.8/99.5
	Grid	100/99.6	97.7/98.8	99.1/99.4	99.9/98.5	100/99.4	100/99.1	100/99.3	100/99.5
	Leather	99.3/99.5	100/99.3	100/99.7	100/99.2	100/99.8	100/99.4	100/99.5	100/99.9
	Tile	100/98.6	98.8/95.7	100/96.7	98.7/97.7	100/99.7	99.3/95.6	99.9/95.7	99.7/96.6
	Wood	94.7/91.5	99.1/95.0	99.5/97.0	99.5/94.4	99.9/98.8	99.2/95.3	99.6/95.5	99.3/95.8
Avg.		98.2/95.8	99.1/98.1	97.9/98.2	99.5/98.1	99.9/99.3	98.5/97.7	99.4/98.0	99.4/98.3

Table 1. Performance comparison across different methods in *one-class* tasks. **Bold text** indicates the best performance among all methods, while underlined text shows the comparison between our improved method and the original method. The values in the form of xx/xx represent *image-level AUROC* / *pixel-level AUROC*.

Category	US [2]	PSVDD [27]	PaDiM [5]	MKD [22]	DRAEM [30]	UniAD [28]	UniAD (+COAD)	DiAD [11]	DiAD (+COAD)
Object	Bottle	84.0/67.9	85.5/86.7	97.9/96.1	98.7/91.8	97.5/87.6	<u>99.7/98.1</u>	100/98.0	99.7/98.4
	Cable	60.0/78.3	64.4/62.2	70.9/81.0	78.2/89.3	57.8/71.3	95.2/97.3	97.9/98.8	94.8/96.8
	Capsule	57.6/85.5	61.3/83.1	73.4/96.9	68.3/88.3	65.3/50.5	86.9/98.5	<u>92.3/98.6</u>	89.0/97.1
	Hazelnut	95.8/93.7	83.9/97.4	85.5/96.3	97.1/91.2	93.7/96.9	<u>99.8/98.1</u>	<u>99.9/98.1</u>	99.5/98.3
	Metal Nut	62.7/76.6	80.9/96.0	88.0/84.8	64.9/64.2	72.8/62.2	99.2/94.8	<u>99.3/93.2</u>	99.1/97.3
	Pill	56.1/80.3	89.4/96.5	68.8/87.7	79.7/69.7	82.2/94.4	93.7/95.0	94.4/98.4	95.7/95.7
	Screw	66.9/90.8	80.9/74.3	56.9/94.1	75.6/92.1	92.0/95.5	87.5/98.3	90.6/98.6	90.7/97.9
	Toothbrush	57.8/86.9	99.4/98.0	95.3/95.6	75.3/88.9	90.6/97.7	94.2/98.4	<u>94.7/98.6</u>	99.7/99.0
	Transistor	61.0/68.3	77.5/78.5	86.6/92.3	73.4/71.7	74.8/64.5	99.8/97.9	99.8/98.4	99.8/95.1
	Zipper	78.6/84.2	77.8/95.1	79.7/94.8	87.4/86.1	98.8/98.3	95.8/96.8	<u>97.6/98.1</u>	95.1/96.2
Texture	Carpet	86.6/88.7	63.3/78.6	93.8/97.6	69.8/95.5	98.0/98.6	99.8/98.5	100/98.8	99.4/98.6
	Grid	69.2/64.5	66.0/70.8	73.9/71.0	83.8/82.3	99.3/98.7	98.2/96.5	<u>99.1/98.4</u>	98.5/96.6
	Leather	97.2/95.4	60.8/93.5	99.9/98.4	93.6/96.7	98.7/97.3	100/98.8	100/98.8	99.8/98.8
	Tile	93.7/82.7	88.3/92.1	93.3/80.5	89.5/85.3	99.8/98.0	99.3/91.8	<u>99.3/98.6</u>	96.8/92.4
	Wood	90.6/83.3	72.1/80.7	98.4/89.1	93.4/80.5	99.8/96.0	98.6/93.2	98.5/96.1	99.7/93.3
Avg.		74.5/81.8	76.8/85.6	84.2/89.5	81.9/84.9	88.1/87.2	96.5/96.8	97.6/98.0	97.2/96.8

Table 2. Performance comparison across different methods in *multi-class* tasks. **Bold text** indicates the best performance among all methods, while underlined text shows the comparison between our improved method and the original method. The values in the form of xx/xx represent *image-level AUROC* / *pixel-level AUROC*.

the same manner as the baseline anomaly detection frameworks, ensuring that the enhancements provided by *COAD* integrate seamlessly.

The results of our *one-class* and *multi-class* experiments are summarized in Tabs. 1 and 2. It can be observed that our enhanced method outperforms the original methods, achieving new **SOTA** results. The enhancement in pixel-level AUROC is especially significant, which is crucial for fine-grained anomaly detection.

These results confirm that the introduction of controllable overfitting, regulated by *ARQ* and *RADI*, enhances the model’s sensitivity and stability, leading to robust anomaly detection abilities that outperform existing **SOTA** methods.

4.3. Ablation Study

4.3.1 Comparisons with Our Basic Frameworks

	RD	RD++	UniAD	DiAD
Baseline	98.5	99.4	96.5	97.2
+COAD	99.4(+0.9)	99.9(+0.5)	97.6(+1.1)	99.1(+1.9)

Table 3. Image-Level AUROC comparison between the basic and enhanced versions of different frameworks.

We conduct an ablation study comparing our enhanced framework with its corresponding basic versions in Tabs. 3 and 4. The results demonstrate consistent and notable improvements in both image-level and pixel-level AUROC

	<i>RD</i>	<i>RD++</i>	<i>UniAD</i>	<i>DiAD</i>
Baseline	97.7	98.3	96.8	96.8
<i>+COAD</i>	98.0(+0.3)	99.4(+1.1)	98.0(+1.2)	98.0(+1.2)

Table 4. Pixel-Level AUROC comparison between the basic and enhanced versions of different frameworks.

across all evaluated frameworks.

In particular, the performance gains observed in image-level anomaly detection emphasize the strength of our *COAD*, which effectively captures subtle differences between normal and anomalous regions. Specifically, our enhancements yielded an increase of up to 1.9 in the *DiAD* framework, as seen in image-level AUROC, and similar significant improvements in other frameworks.

For pixel-level AUROC, a similar pattern of improvement was observed, with gains of up to 1.2 seen in multiple frameworks, as shown in Tab. 4. This underscores the strength of our *COAD*, which not only optimizes image-level detection but also provides enhanced granularity in distinguishing pixel-level abnormalities.

Furthermore, the versatility of our method is evident in its applicability to different anomaly detection paradigms. Whether in *one-class* or *multi-class* anomaly detection tasks, or even in settings employing *diffusion-based* models versus *non-diffusion* frameworks, our method has consistently demonstrated superior performance, showcasing our method’s robustness and generalizability.

4.3.2 Comparisons with Distinct *ARQ*

Model	0–0.001	0.001–0.011	0.011–0.1
<i>RD</i>	98.8 / 97.8	99.4 / 98.0	99.6 / 97.6
<i>RD++</i>	99.7 / 98.8	99.9 / 99.4	-

Table 5. Comparison of performance across distinct *ARQ* ranges for different models in *one-class* tasks.

Model	0–0.01	0.01–0.11	0.11–1
<i>UniAD</i>	97.0 / 96.8	97.6 / 98.0	98.1 / 96.9
<i>DiAD</i>	97.3 / 96.6	99.1 / 98.0	99.2 / 96.5

Table 6. Comparison of performance across distinct *ARQ* ranges for different models in *multi-class* tasks.

In this section, we compare the performance of different models under distinct *ARQ* ranges to validate the impact of controllable overfitting on anomaly detection. We evaluated methods such as *RD*, *RD++*, *UniAD*, and *DiAD*

across various *ARQ* levels. As Tabs. 5 and 6 show, the results demonstrate that, by appropriately regulating the *ARQ*, which is in $ARQ_{optimal}$, model detection performance can be significantly enhanced. It is evident that our controllable overfitting strategy not only yields consistent improvements across different models but also helps in striking the optimal balance between overfitting and generalization.

Overall, these results demonstrate that our controllable overfitting strategy consistently yields significant performance gains across various models and tasks. By leveraging the *ARQ* within the identified optimal range, we successfully enhance the models’ discriminative abilities while maintaining a balanced relationship between overfitting and generalization.

4.4. Validation of Distribution Assumptions and Theoretical Validation of Gaussian Noise Usage

<i>ARQ</i>	μ_n	θ_n	μ_a	θ_a	<i>TVD</i> _{<i>n</i>}	<i>TVD</i> _{<i>a</i>}
0	105.6	65.5	99.3	45.0	0.20	0.08
0.006	105.3	65.5	98.9	44.9	0.20	0.08
0.015	105.6	65.5	99.0	45.1	0.20	0.08
0.045	105.8	65.4	99.3	45.1	0.20	0.08
0.050	105.6	65.3	99.1	45.0	0.21	0.09
0.060	105.6	65.2	99.0	45.0	0.20	0.09
0.082	105.5	65.0	99.0	45.0	0.19	0.08

Table 7. Partial Results of Validation Metrics for Assumptions on Normal and Anomalous Pixel Score Distributions.

In this section, we firstly validate the assumptions introduced in Sec. 3.3.1 by employing the Total Variation Distance (TVD) metric. We leveraging multiple models at different stages of overfitting, characterized by distinct *ARQ* values. For each model state, corresponding to different $ARQ = \theta$, we calculate the prediction scores for both normal and anomalous pixels across the dataset. Subsequently, we evaluate their proximity to a Gaussian distribution using TVD, ensuring a robust assessment of the normality of these distributions. The partial results of this validation are summarized in Tab. 7. Moreover, we model the variance of the normal pixel prediction scores ($\sigma_n(\theta)$) as an exponential function of the $ARQ = \theta$, given by Eq. (4).

To validate the suitability of Gaussian noise as a pseudo-anomaly generator, we employ the TVD metric to quantitatively compare the distribution of real anomaly scores with that of Gaussian-distributed pseudo-anomalies. We can see Tab. 7, the resulting TVD value was about **0.08**, suggesting that the Gaussian-distributed pseudo-anomalies exhibit a significant overlap with the actual anomalies. This supports the assumptions that Gaussian noise can be effectively used to preliminarily simulate anomalous behavior in train-

ing models for anomaly detection, which is usually used by *GLASS*[4], *SimpleNet*[17], *RealNet*[32], and *DDPM* [12].

5. Conclusion

In this work, we reenvisioned overfitting as a controllable and transformative mechanism, using *COAD* to enhance model capabilities beyond conventional boundaries. We introduced *ARQ* to precisely regulate overfitting, as well as *RADI*, which leverages $ARQ_{optimal}$ to provide a more versatile metric compared to *AUROC-pixel*, facilitating both theoretical modeling and *Dual Control Mechanism*. By repurposing overfitting as a generalizable module, our approach not only dismantles its demonization but also enables us to achieve SOTA results in both *one-class* and *multi-class* anomaly detection tasks. Furthermore, we provide a robust theoretical foundation for employing Gaussian noise as a preliminary pseudo-anomaly generator, extending the applicability of our *COAD*.

References

- [1] Paul Bergmann, Michael Fauser, David Sattlegger, and Carsten Steger. Mvtex ad—a comprehensive real-world dataset for unsupervised anomaly detection. In *Proceedings of the IEEE/CVF conference on computer vision and pattern recognition*, pages 9592–9600, 2019. 6
- [2] Paul Bergmann, Michael Fauser, David Sattlegger, and Carsten Steger. Uninformed students: Student-teacher anomaly detection with discriminative latent embeddings. In *Proceedings of the IEEE/CVF Conference on Computer Vision and Pattern Recognition (CVPR)*, 2020. 7
- [3] Christopher Bishop. *Pattern Recognition and Machine Learning*. Springer, 2006. 1
- [4] Qiyu Chen, Huiyuan Luo, Chengkan Lv, and Zhengtao Zhang. A unified anomaly synthesis strategy with gradient ascent for industrial anomaly detection and localization, 2024. 2, 3, 7, 9, 4
- [5] Thomas Defard, Aleksandr Setkov, Angelique Loesch, and Romaric Audigier. Padim: A patch distribution modeling framework for anomaly detection and localization. In *Pattern Recognition. ICPR International Workshops and Challenges*, pages 475–489, Cham, 2021. Springer International Publishing. 7
- [6] Hanqiu Deng and Xingyu Li. Anomaly detection via reverse distillation from one-class embedding. In *Proceedings of the IEEE/CVF Conference on Computer Vision and Pattern Recognition (CVPR)*, pages 9737–9746, 2022. 1, 2, 3, 7
- [7] Ian Goodfellow, Jean Pouget-Abadie, Mehdi Mirza, Bing Xu, David Warde-Farley, Sherjil Ozair, Aaron Courville, and Y. Bengio. Generative adversarial nets. *MIT Press*, 2014. 2
- [8] Ian Goodfellow, Yoshua Bengio, and Aaron Courville. *Deep Learning*. MIT Press, 2016. <http://www.deeplearningbook.org>. 1
- [9] Denis Gudovskiy, Shun Ishizaka, and Kazuki Kozuka. Cflow-ad: Real-time unsupervised anomaly detection with localization via conditional normalizing flows, 2021. 2, 3
- [10] Trevor Hastie, Robert Tibshirani, Jerome Friedman, and James Franklin. The elements of statistical learning: Data mining, inference, and prediction. *Math. Intell.*, 27:83–85, 2004. 1
- [11] Haoyang He, Jiangning Zhang, Hongxu Chen, Xuhai Chen, Zhishan Li, Xu Chen, Yabiao Wang, Chengjie Wang, and Lei Xie. Diad: A diffusion-based framework for multi-class anomaly detection, 2023. 1, 3, 7
- [12] Jonathan Ho, Ajay Jain, and Pieter Abbeel. Denoising diffusion probabilistic models. *Advances in neural information processing systems*, 33:6840–6851, 2020. 3, 9
- [13] Jiarui Lei, Xiaobo Hu, Yue Wang, and Dong Liu. Pyramid-flow: High-resolution defect contrastive localization using pyramid normalizing flow, 2023. 2, 3
- [14] Chun Liang Li, Kihyuk Sohn, Jinsung Yoon, and Tomas Pfister. Cutpaste: Self-supervised learning for anomaly detection and localization, 2021. 3
- [15] Yufei Liang, Jiangning Zhang, Shiwei Zhao, Runze Wu, Yong Liu, and Shuwen Pan. Omni-frequency channel-selection representations for unsupervised anomaly detection. *IEEE Transactions on Image Processing*, 32:4327–4340, 2023. 2
- [16] Xinyue Liu, Jianyuan Wang, Biao Leng, and Shuo Zhang. Dual-modeling decouple distillation for unsupervised anomaly detection. *arXiv preprint arXiv:2408.03888*, 2024. 3
- [17] Zhikang Liu, Yiming Zhou, Yuansheng Xu, and Zilei Wang. Simplenet: A simple network for image anomaly detection and localization. In *Proceedings of the IEEE/CVF Conference on Computer Vision and Pattern Recognition (CVPR)*, pages 20402–20411, 2023. 2, 3, 7, 9
- [18] Ruiying Lu, YuJie Wu, Long Tian, Dongsheng Wang, Bo Chen, Xiyang Liu, and Ruimin Hu. Hierarchical vector quantized transformer for multi-class unsupervised anomaly detection. *Advances in Neural Information Processing Systems*, 36:8487–8500, 2023. 3
- [19] Henry B Mann and Donald R Whitney. On a test of whether one of two random variables is stochastically larger than the other. *The annals of mathematical statistics*, pages 50–60, 1947. 5
- [20] Kevin P Murphy. *Machine learning: a probabilistic perspective*. Cambridge, MA, 2012. 1
- [21] Karsten Roth, Latha Pemula, Joaquin Zepeda, Bernhard Schölkopf, Thomas Brox, and Peter Gehler. Towards total recall in industrial anomaly detection. In *Proceedings of the IEEE/CVF Conference on Computer Vision and Pattern Recognition (CVPR)*, pages 14318–14328, 2022. 7
- [22] Mohammadreza Salehi, Niousha Sadjadi, Soroosh Baselizadeh, Mohammad H. Rohban, and Hamid R. Rabiee. Multiresolution knowledge distillation for anomaly detection. In *Proceedings of the IEEE/CVF Conference on Computer Vision and Pattern Recognition (CVPR)*, pages 14902–14912, 2021. 7
- [23] Tran Dinh Tien, Anh Tuan Nguyen, Nguyen Hoang Tran, Ta Duc Huy, Soan T.M. Duong, Chanh D. Tr. Nguyen, and Steven Q. H. Truong. Revisiting reverse distillation for anomaly detection. In *Proceedings of the IEEE/CVF Conference on Computer Vision and Pattern Recognition (CVPR)*, pages 14913–14923, 2021. 7

- ence on Computer Vision and Pattern Recognition (CVPR), pages 24511–24520, 2023. [1](#), [2](#), [3](#), [7](#)
- [24] Frank Wilcoxon. Individual comparisons by ranking methods. In *Breakthroughs in statistics: Methodology and distribution*, pages 196–202. Springer, 1992. [5](#)
- [25] Feng Xiao, Ruoyu Sun, and Jicong Fan. Restricted generative projection for one-class classification and anomaly detection, 2023. [2](#), [3](#)
- [26] Xincheng Yao, Ruoci Li, Jing Zhang, Jun Sun, and Chongyang Zhang. Explicit boundary guided semi-push-pull contrastive learning for supervised anomaly detection. In *Proceedings of the IEEE/CVF Conference on Computer Vision and Pattern Recognition (CVPR)*, pages 24490–24499, 2023. [7](#)
- [27] Jihun Yi and Sungroh Yoon. Patch svdd: Patch-level svdd for anomaly detection and segmentation. In *Proceedings of the Asian Conference on Computer Vision (ACCV)*, 2020. [7](#)
- [28] Zhiyuan You, Lei Cui, Yujun Shen, Kai Yang, Xin Lu, Yu Zheng, and Xinyi Le. A unified model for multi-class anomaly detection, 2022. [1](#), [2](#), [3](#), [7](#)
- [29] Danijel Zavrtanik, Matej Skočaj. Reconstruction by inpainting for visual anomaly detection. *Pattern Recognition: The Journal of the Pattern Recognition Society*, 112(1), 2021. [2](#)
- [30] Vitjan Zavrtanik, Matej Kristan, and Danijel Skočaj. Draem – a discriminatively trained reconstruction embedding for surface anomaly detection. In *Proceedings of the IEEE/CVF International Conference on Computer Vision (ICCV)*, pages 8330–8339, 2021. [2](#), [3](#), [7](#)
- [31] Vitjan Zavrtanik, Matej Kristan, and Danijel Skočaj. Dsr – a dual subspace re-projection network for surface anomaly detection. In *Computer Vision – ECCV 2022*, pages 539–554, Cham, 2022. Springer Nature Switzerland. [2](#), [7](#)
- [32] Ximiao Zhang, Min Xu, and Xiuzhuang Zhou. Realnet: A feature selection network with realistic synthetic anomaly for anomaly detection, 2024. [2](#), [3](#), [9](#)
- [33] Yibo Zhou. Rethinking reconstruction autoencoder-based out-of-distribution detection. 2022. [2](#)

Friend or Foe? Harnessing Controllable Overfitting for Anomaly Detection

Supplementary Material

6. Dual Control Mechanism Design Concept

Overfitting has traditionally been viewed as a problem that hampers generalization—where the model memorizes noise and specific details of the training data, leading to poor performance on unseen examples. However, in the context of anomaly detection, we posit that overfitting can be harnessed as a *feature*, not a flaw. The key lies in the concept of *controllable overfitting*—managing overfitting in a way that makes the model more sensitive to subtle differences between normal and anomalous data.

In practical terms, overfitting can amplify the sensitivity of the model to slight deviations, which is particularly useful in anomaly detection scenarios, where anomalies are often defined by subtle discrepancies from the norm. Our approach aims to leverage this characteristic to enhance detection capability while avoiding the negative consequences of overfitting, such as loss of generalization. This balancing act necessitates a carefully designed mechanism, which we call the *Dual Control Mechanism* in Eq. (14).

The **Dual Control Mechanism** is comprised of two complementary components: $ARQ_{optimal}$ in Eq. (2) and *Gradient-Guided Overfitting Control* in Eq. (13). These components work together to ensure that overfitting remains within beneficial bounds, ultimately enhancing anomaly detection without sacrificing the ability to generalize effectively.

Aberrance Retention Quotient The ARQ quantifies the degree of overfitting by capturing the relationship between the model’s fit to the training data and its potential for retaining useful deviations that indicate anomalies. We define an optimal interval for ARQ , denoted as $ARQ_{optimal}$, which represents the range where overfitting is beneficial—significantly enhancing sensitivity to anomalies without compromising generalization.

During training, ARQ is continuously monitored to ensure it remains within this optimal interval. If ARQ moves outside the defined range, corrective actions are taken to bring it back. The optimal interval allows the model to exploit overfitting in a targeted manner, enhancing the model’s sensitivity towards subtle anomalies while minimizing the risk of memorizing noise.

Gradient-Guided Overfitting Control Alongside $ARQ_{optimal}$, the *Gradient-Guided Overfitting Control* is employed to supervise how overfitting impacts anomaly detection performance directly. This component utilizes the *Relative Anomaly Distribution Index* ($RADI$) to quantify the

overlap between normal and anomalous score distributions. By keeping track of the gradient of $RADI$, we can ensure that the anomaly detection performance is on an upward trajectory during overfitting.

Specifically, we require that the gradient of $RADI$ with respect to ARQ is non-negative, which indicates that the model’s ability to distinguish anomalies from normal data is improving as overfitting increases. If the gradient condition is violated, indicating that overfitting is leading to a decline in detection performance, additional measures are triggered.

Freeze Command Signals for Progressive Layer Freezing In situations where the *Dual Control Mechanism* fails—meaning both the ARQ exceeds the optimal range and the *Gradient-Guided Overfitting Control* shows deteriorating performance—we initiate *Freeze Command Signals* in. These signals are the model’s way of mitigating excessive overfitting by progressively freezing network layers.

Freeze Command Signals begin by selectively freezing the lower-level feature extraction layers, which are primarily responsible for capturing fundamental visual features such as edges, textures, and basic shapes. These foundational features are generally invariant across different images and therefore require less flexibility once they are well-trained. By freezing these lower-level layers, we stabilize the feature extraction process, reducing the risk of the model overfitting to noise and minute variations in the training set. As training progresses and overfitting persists beyond the optimal range, additional higher-level layers are frozen progressively in a staged manner. This gradual freezing strategy ensures that while the foundational layers remain stable, the more abstract, task-specific layers retain flexibility long enough to refine their understanding of anomalies.

By progressively freezing layers, the model maintains stable low-level feature extraction while allowing the higher-level layers to refine their understanding of anomalies. This approach ensures that the model retains a balance between maintaining its basic feature extraction capabilities and enhancing its discriminative power for anomaly detection.

The **Dual Control Mechanism** thus provides a comprehensive way to manage overfitting during training. By monitoring both ARQ and the $RADI$ gradient, and employing *Freeze Command Signals* when necessary, our framework transforms overfitting from a challenge into an asset—amplifying the model’s ability to detect anomalies while maintaining robustness and generalization.

7. Main Functional Pseudocode

Algorithm 1 Training Stage with Gaussian Noise, Teacher-Student Reconstruction, and Overfitting Control

Require: Dataset \mathcal{D} , Initial Model M , Learning Rate α , Optimal ARQ Range $\theta_{optimal}$, Noise Standard Deviation σ_{noise} , Epochs $N_{standard}$, Overfit Epochs $N_{overfit}$

1: **Step 1: Standard Training Stage**
2: **for** epoch = 1 to $N_{standard}$ **do**
3: **for** batch in \mathcal{D}_{train} **do**
4: Generate pseudo-anomalous data $\mathcal{D}_{anomaly}$ using Gaussian noise.
5: Generate feature maps F_T using the Teacher Model M_T for training samples.
6: Generate reconstructed feature maps F_S using the Student Model M_S .
7: Compute $L_{reconstruction}$ between F_T and F_S and other losses.
8: Update Models
9: **end for**
10: **end for**
11: **Step 2: Controllable Overfitting Stage**
12: Set learning rate $\alpha_{overfit} = \alpha/10$
13: Initialize Freeze Counter $C = 0$
14: **for** epoch = 1 to $N_{overfit}$ **do**
15: **for** batch in \mathcal{D}_{train} **do**
16: Generate pseudo-anomalous data $\mathcal{D}_{anomaly}$ using Gaussian noise.
17: Generate feature maps F_T using the Teacher Model M_T for both normal and pseudo-anomalous samples.
18: Generate reconstructed feature maps F_S using the Student Model M_S .
19: Calculate ARQ
20: Compute RADI based on score distributions
21: **Dual Control Mechanism:**
22: **if** θ exceeds $\theta_{optimal}$ or $\frac{dRADI(\theta)}{d\theta} < 0$ **then**
23: Increment Freeze Counter C
24: **if** $C > C_{thr}$ **then**
25: Issue *Freeze Command Signals*
26: **Selective Freezing**
27: **end if**
28: **else**
29: Reset Freeze Counter C
30: **end if**
31: Compute $L_{reconstruction}$ between F_T and F_S and other losses.
32: Update Models
33: **end for**
34: **end for**

Algorithm 2 Selective Freezing

Require: Student Model M_S , Freeze Counter C , Threshold C_{max} , Layer List L , ARQ θ , Optimal ARQ Range $\theta_{optimal}$

1: Initialize $C = 0$ {Freeze Counter initialized to zero}
2: **for** epoch = 1 to $N_{overfit}$ **do**
3: **for** batch in training data **do**
4: Perform forward pass and compute ARQ θ
5: **if** θ exceeds $\theta_{optimal}$ **or** $\frac{dRADI(\theta)}{d\theta} < 0$ **then**
6: Increment Freeze Counter: $C = C + 1$
7: **else**
8: Reset Freeze Counter: $C = 0$
9: **end if**
10: **if** $C > C_{thr}$ **then**
11: Issue *Freeze Command Signal* to initiate layer freezing
12: **Layer Freezing Process:**
13: **for** layer l in L (ordered from lowest-level to highest-level) **do**
14: **if** layer l is not frozen **then**
15: **Freeze Procedure for Current Layer:**
16: $\forall p \in$ parameters of layer l
17: $p.requires_grad = \text{False}$ {Stop gradient updates for layer l }
18: Update training status: mark layer l as *frozen*
19: **Apply Forward Freezing Effects:**
20: Notify subsequent layers in network to adjust activations {Maintain balance during backpropagation}
21: Update batch normalization layers if necessary {Handle training vs. inference mode}
22: Reset Freeze Counter: $C = 0$ {Reset counter after successfully freezing a layer}
23: Add layer l to the Frozen Layer List F {Keep track of all frozen layers}
24: **Break** from the loop {Freeze only one layer in each iteration to avoid rapid performance drops}
25: **else**
26: **Continue** to next layer {Skip if layer is already frozen}
27: **end if**
28: **end for**
29: **end if**
30: **Continue Training:**
31: Perform backpropagation and update weights accordingly
32: **end for**
33: **end for**

Algorithm 3 Inference Stage

Require: Trained Teacher Model M_{teacher} , Trained Student Model M_{student} , Test Dataset $\mathcal{D}_{\text{test}}$, Optional Pseudo Anomaly Filter F

- 1: **Initialization:** Set models in evaluation mode.
- 2: **for** test sample x in $\mathcal{D}_{\text{test}}$ **do**
- 3: **Input Feature Extraction:**
- 4: Extract features using teacher model: $f_{\text{teacher}} \leftarrow M_{\text{teacher}}(x)$
- 5: **Student Model Inference:**
- 6: Extract reconstructed features using student model: $\hat{f}_{\text{student}} \leftarrow M_{\text{student}}(f_{\text{filtered}})$
- 7: **Reconstruction Computation:**
- 8: Compute reconstruction error to classify sample: $e(x) = \text{Loss}(x, \hat{f}_{\text{student}})$
- 9: **Prediction Generation:**
- 10: **if** $e(x) > \text{Threshold}$ **then**
- 11: Classify as **Anomalous**
- 12: **else**
- 13: Classify as **Normal**
- 14: **end if**
- 15: **Store Results:** Save prediction results for sample x .
- 16: **end for**
- 17: **Output:** Anomaly classification for all test samples in $\mathcal{D}_{\text{test}}$

Algorithm 4 Calculation of Aberrance Retention Quotient (ARQ)

Require: Predicted values \hat{y}_i , Ground truth values y_i , Total instances N

- 1: Initialize ARQ value: $ARQ \leftarrow 0$
- 2: **Compute Numerator:**
- 3: $\text{Numerator} \leftarrow \sum_{i=1}^N |\hat{y}_i - y_i|$
- 4: **Compute Denominator:**
- 5: $\text{Denominator} \leftarrow \sum_{i=1}^N y_i$
- 6: **Calculate ARQ:**
- 7: $ARQ \leftarrow \frac{\text{Numerator}}{\text{Denominator}}$
- 8: **Output:** Final ARQ value

Algorithm 5 Calculation of Relative Anomaly Distribution Index (RADI)

Require: Scores of anomalous pixels S_a , Scores of normal pixels S_n

- 1: Initialize $RADI$ value: $RADI \leftarrow 0$
- 2: **Compute RADI using Integral:**
- 3: $RADI \leftarrow \int_{-\infty}^{\infty} P(S_a > x) \cdot f_{S_n}(x) dx$
- 4: **Output:** Final $RADI$ value

8. Extended Discussion of Gaussian Noise Validation

8.1. Theoretical Rationale for Gaussian Noise

In this work, we chose to use Gaussian noise as a preliminarily pseudo-anomaly generator due to its statistical properties and simplicity. Gaussian noise, characterized by its mean and variance, serves as an ideal candidate for generating random deviations that can mimic unexpected patterns in normal data.

From a theoretical standpoint, Gaussian noise exhibits a distribution that is both isotropic and well-defined in high-dimensional space, making it suitable for approximating unstructured, irregular anomalies. The Central Limit Theorem (CLT) supports the use of Gaussian distributions as approximations for many naturally occurring random processes. In particular, when adding minor perturbations to an image, we aim to simulate unforeseen deviations from the underlying structure of normal samples, which Gaussian noise effectively captures.

Additionally, Gaussian noise serves as a zero-mean stochastic process, allowing us to avoid introducing any specific directional bias, which could potentially interfere with the model's capacity to learn anomalous versus normal regions. By employing Gaussian noise, we ensure that our model does not overfit to particular anomaly patterns but instead gains a generalized sensitivity to any divergence from the normal data distribution. This universality underpins our approach to controllable overfitting within the *COAD* framework.

8.2. Validation Through Total Variation Distance (TVD)

To validate the suitability of Gaussian noise as a pseudo-anomaly generator, we conducted an empirical analysis using the *Total Variation Distance* (TVD) metric. TVD is a standard measure used in probability theory to quantify the dissimilarity between two distributions. We calculated TVD to evaluate how closely Gaussian noise could mimic true anomalies in both spatial and intensity domains.

The calculation of TVD involves estimating the difference between the empirical distributions of Gaussian noise and the true normal and anomaly pixel intensities:

$$D_{\text{TVD}}(P, Q) = \frac{1}{2} \sum_x |P(x) - Q(x)|, \quad (15)$$

where P represents the empirical distribution of the true anomalies, and Q represents the empirical distribution of Gaussian noise. TVD measures the extent of overlap between the two distributions, where a smaller TVD implies a closer approximation between the pseudo-anomalies and real anomalies.

We conducted experiments on our dataset using both generated Gaussian noise and real anomalies. presents a comparison of the TVD values for different classes. The results indicate that the Gaussian distribution closely matches the distribution of real normal and anomalies across a range of classes. Specifically, it can be seen in Sec. 4.4.

8.3. Experimental Results and Qualitative Study

The experimental results demonstrate that the model trained using Gaussian noise exhibits a better anomaly detection performance to models trained with other pseudo-anomaly generator.

To further validate the results, we present detailed histograms for the anomaly detection scores obtained across 15 individual categories as well as the overall dataset. These histograms were generated under the condition where the *Anomaly Rate Quotient (ARQ)* is set to 0.006, using *RD++* as our baseline framework. Each histogram in Figs. 3 and 4 provides a clear visualization of the distribution of detection scores, overlaid with a Gaussian fitting curve for enhanced interpretability. This fitting curve highlights the distribution, allowing for a more effective comparison of the model’s performance across different categories and the overall dataset, further solidifying the reliability of our evaluation metrics.

8.4. Future Directions with GLASS-like Pseudo-Anomaly Generators

While Gaussian noise has proven effective as a preliminary pseudo-anomaly generator, future work could explore more advanced methods inspired by the *GLASS* approach [4]. The *GLASS* method introduces a structured way to generate pseudo-anomalies by leveraging geometric transformations and localized pattern synthesis, providing greater control over anomaly characteristics.

By incorporating concepts from *GLASS*, we envision a *Gaussian Noise-Enhanced GLASS-like Generator*, where Gaussian noise could act as the foundational perturbation, and additional constraints or transformations could be applied to shape the pseudo-anomalies in a contextually relevant manner. For instance, augmenting Gaussian noise with spatial or intensity correlations reflective of real anomalies could enhance its realism and improve model robustness in detecting diverse anomalies.

Such an approach would align well with our *COAD* framework, enabling a more versatile training process that accounts for both unstructured and structured anomaly patterns. By systematically integrating these future developments, we aim to refine our anomaly detection strategy, bridging the gap between theoretical advancements and practical applications.

9. Qualitative Comparison of Anomaly Detection between Different Baselines and COAD

To further validate the effectiveness of our methods, we provide a qualitative comparison of anomaly detection results across 15 distinct categories using baselines such as *RD*, *RD++*, *UniAD*, *DiAD*, and the proposed *COAD* framework in Figs. 5 to 8. Each subfigure demonstrates: (from left to right) the original image, the ground truth anomaly mask, the result from the baseline method, and the result after applying *COAD*.

The comparison shows that *COAD* effectively reduces both false positive rates (FPR) and false negative rates (FNR), accurately capturing anomaly regions while minimizing misclassifications. These results are consistent with the improvements reflected in the earlier quantitative data in Tabs. 3 and 4, where *COAD* consistently outperforms its counterparts in image-level and pixel-level AUROC metrics, highlighting *COAD*’s capability to outperform the baselines.

By leveraging controllable overfitting, *COAD* enhances the model’s sensitivity to true anomalies while maintaining its generalization capabilities. The reduction in FPR minimizes the misclassification of normal regions as anomalies, while the decreased FNR highlights the model’s ability to capture subtle anomalies that baseline methods often miss. These qualitative and quantitative improvements collectively demonstrate the robustness and effectiveness of *COAD* in advancing anomaly detection tasks. Additionally, the sharper distinction between normal and anomalous regions demonstrates the framework’s capacity to refine boundary precision, further enhancing detection reliability.

10. Future Work

In future work, we plan to refine our pseudo-anomaly generators by incorporating advanced methods in Sec. 8.4, enabling the generation of more structured and domain-relevant pseudo-anomalies.

Moreover, we intend to explore the application of the *COAD* framework in other domains, particularly in areas such as medical imaging, autonomous driving, and forgery detection. Forgery detection, for instance, highlights an opportunity to utilize *COAD*’s enhanced sensitivity to subtle anomalies, such as fine-grained pattern inconsistencies or texture deviations. Furthermore, we aim to generalize and modularize the *COAD* framework into a plug-and-play component that can be seamlessly integrated into similar tasks across various fields. Ultimately, we aspire to redefine the concept of overfitting itself, transforming it from a perceived limitation into a powerful tool that drives innovation.

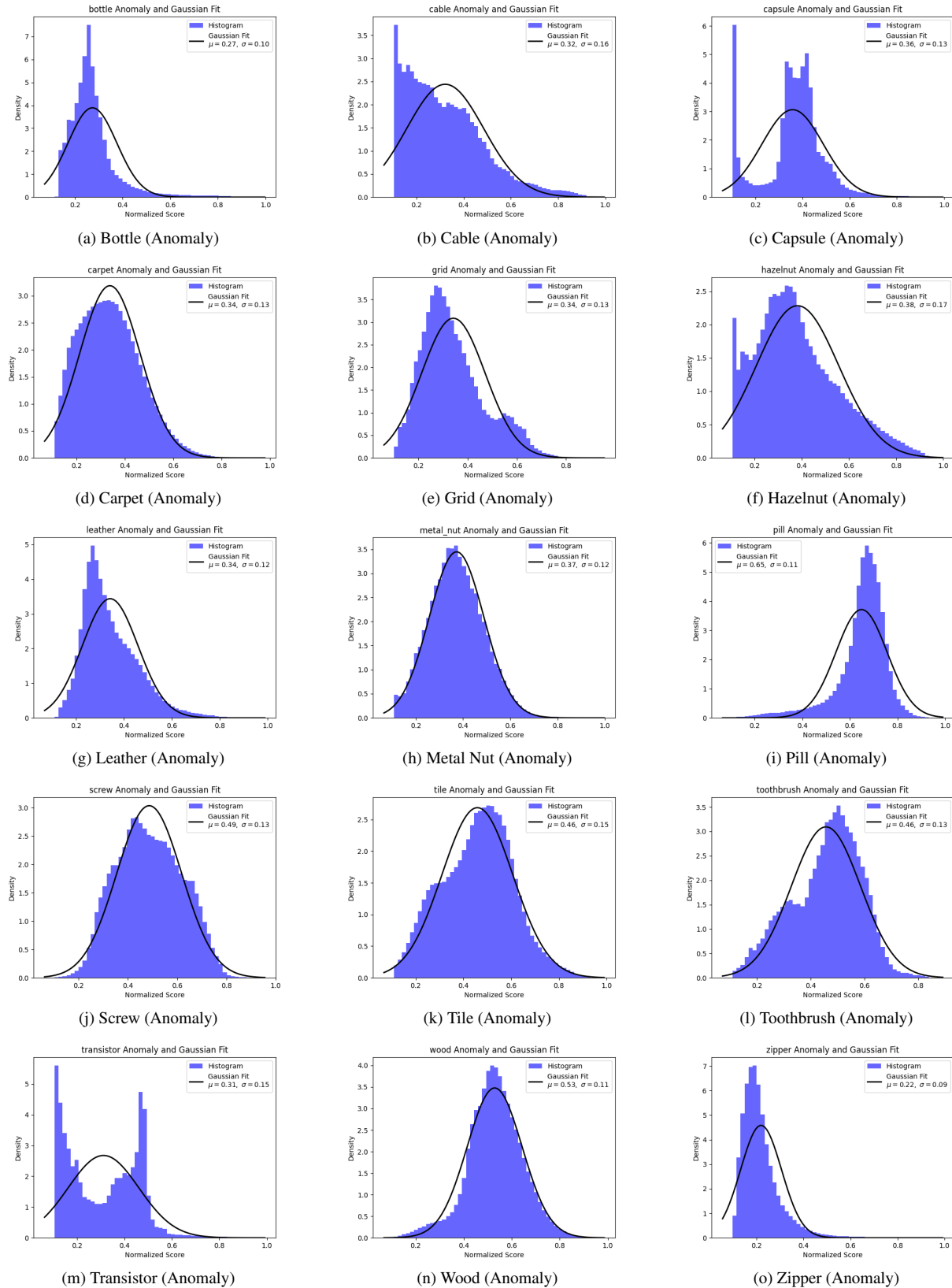


Figure 3. Histograms for anomaly scores of 15 individual categories. Each histogram includes Gaussian fitting curves for better visualization.

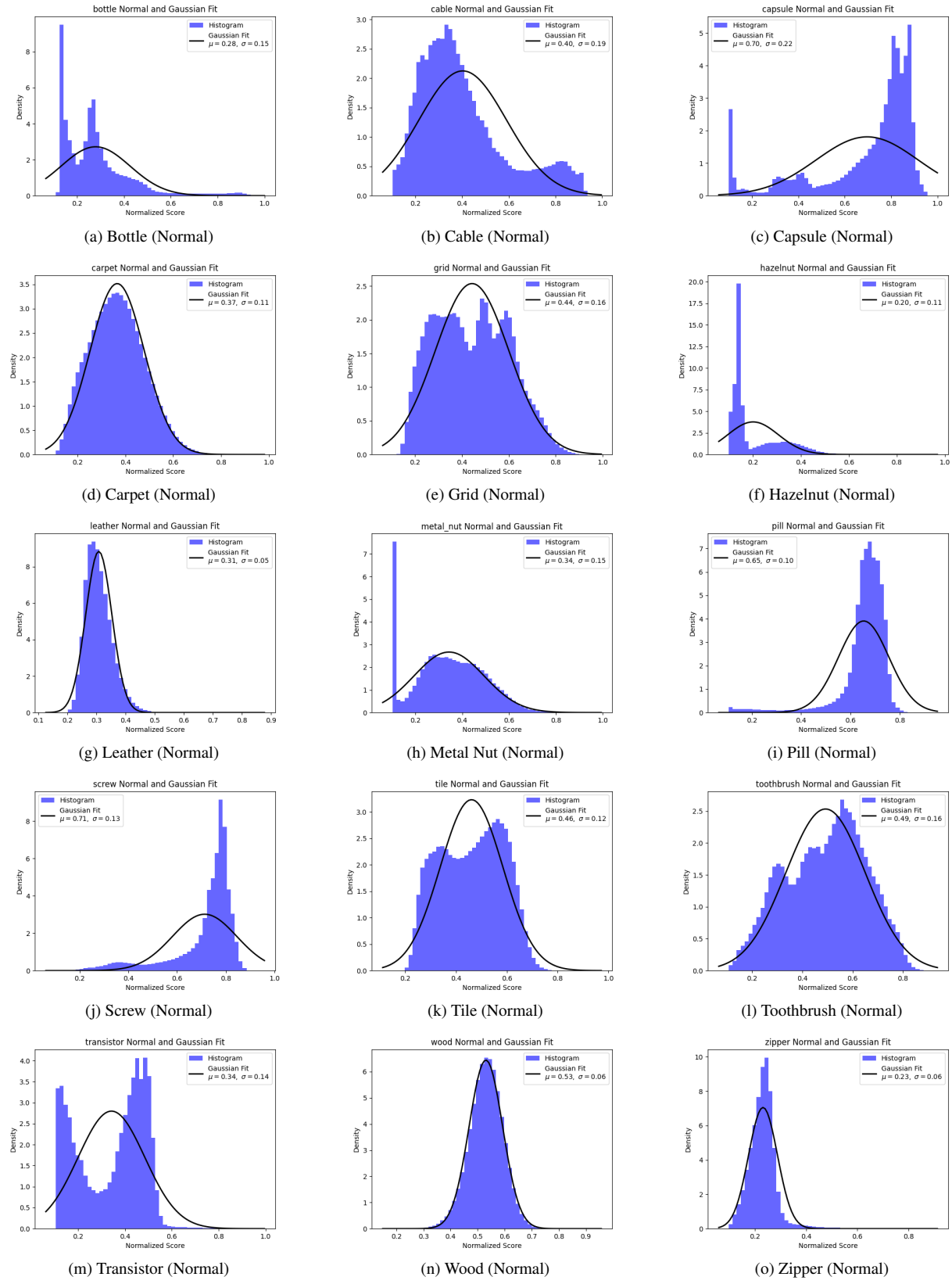


Figure 4. Histograms for normal scores of 15 individual categories. Each histogram includes Gaussian fitting curves for better visualization.

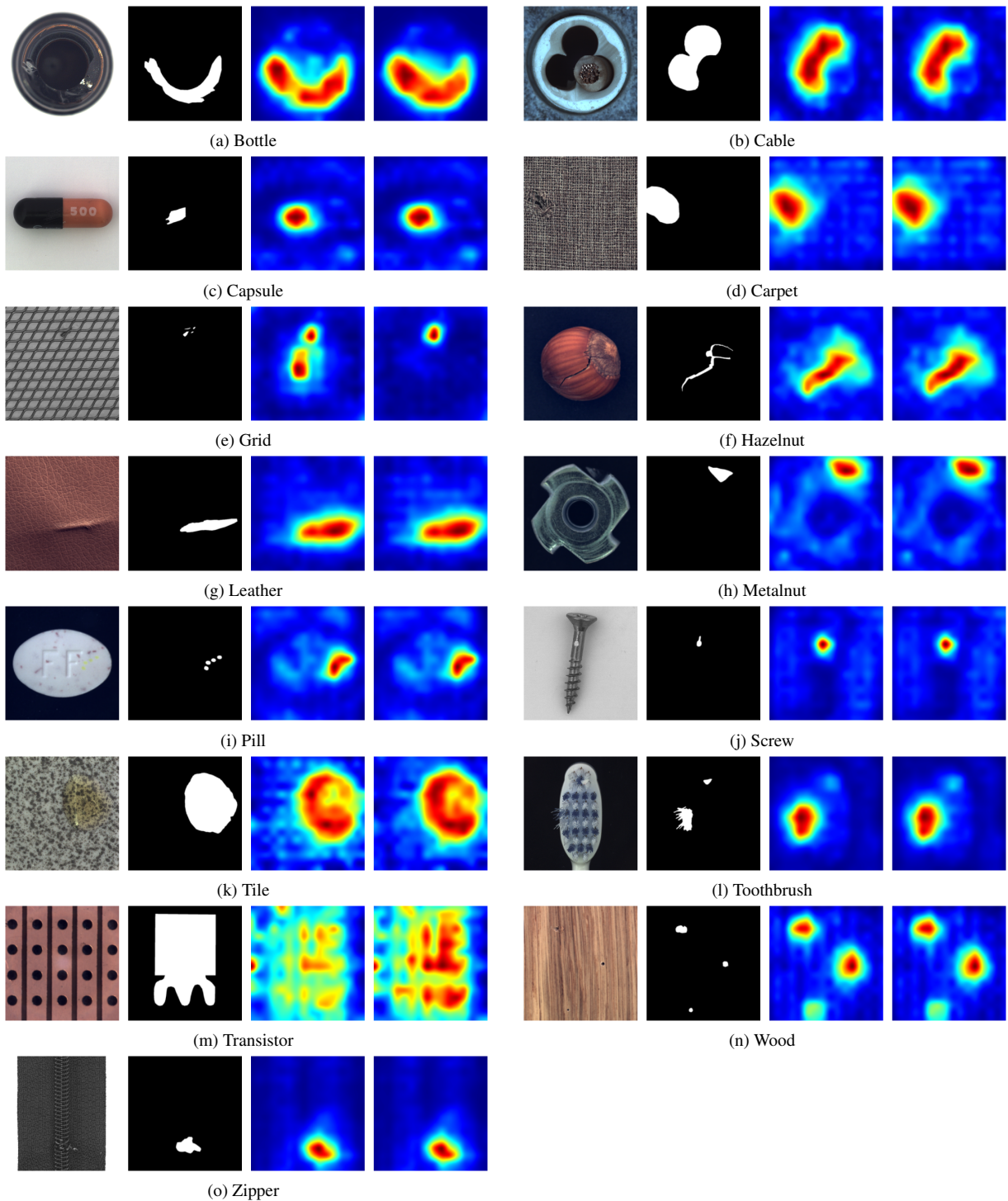


Figure 5. Qualitative Comparison of Anomaly Detection Results Across 15 Categories Using the Baseline Method *RD* and *COAD*. Each subfigure shows: (from left to right) the original image, ground truth, result from the baseline method, and the result after applying *COAD*.

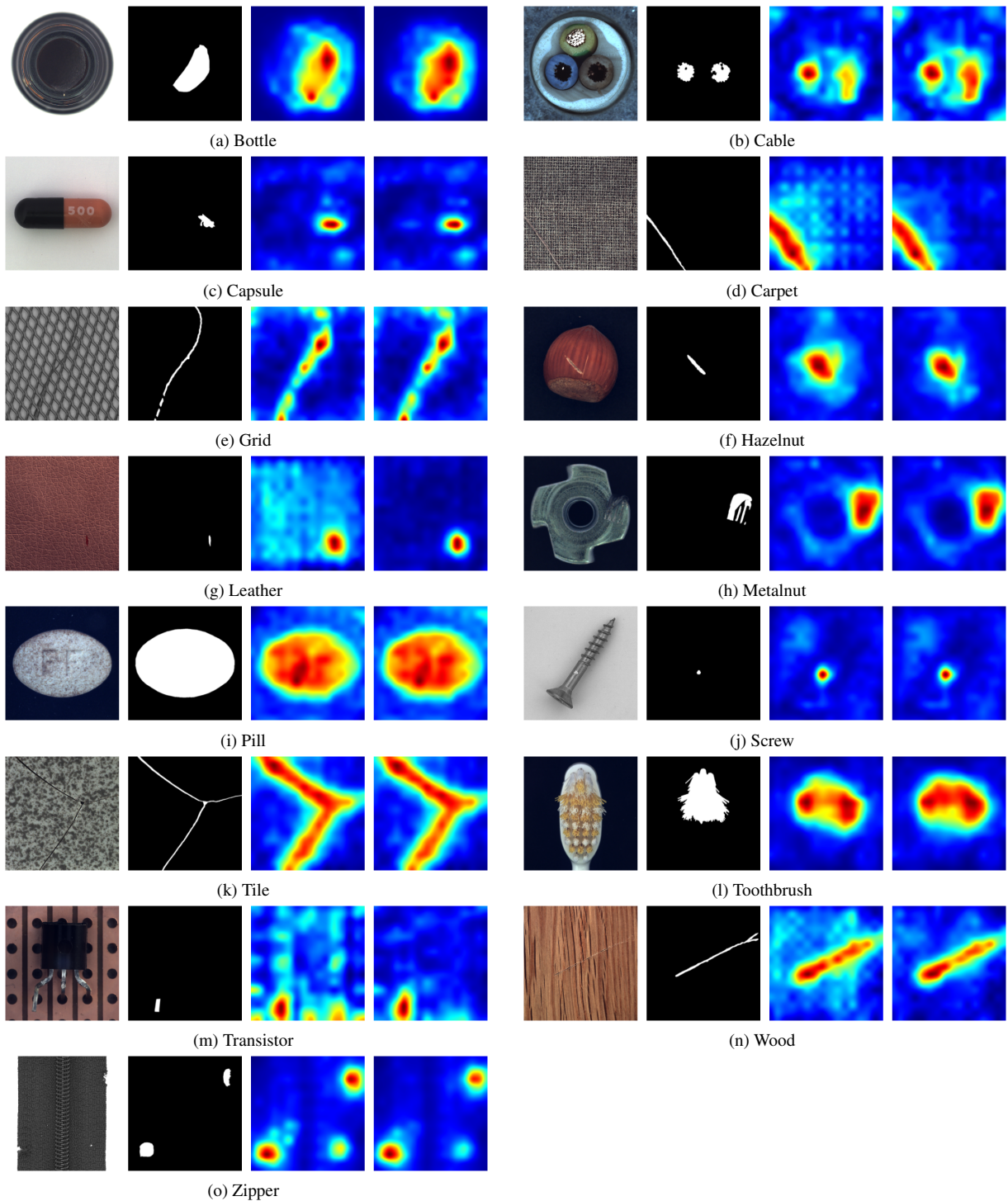


Figure 6. Qualitative Comparison of Anomaly Detection Results Across 15 Categories Using a Baseline Method *RD++* and *COAD*. Each subfigure shows: (from left to right) the original image, ground truth, result from the baseline method, and the result after applying *COAD*.

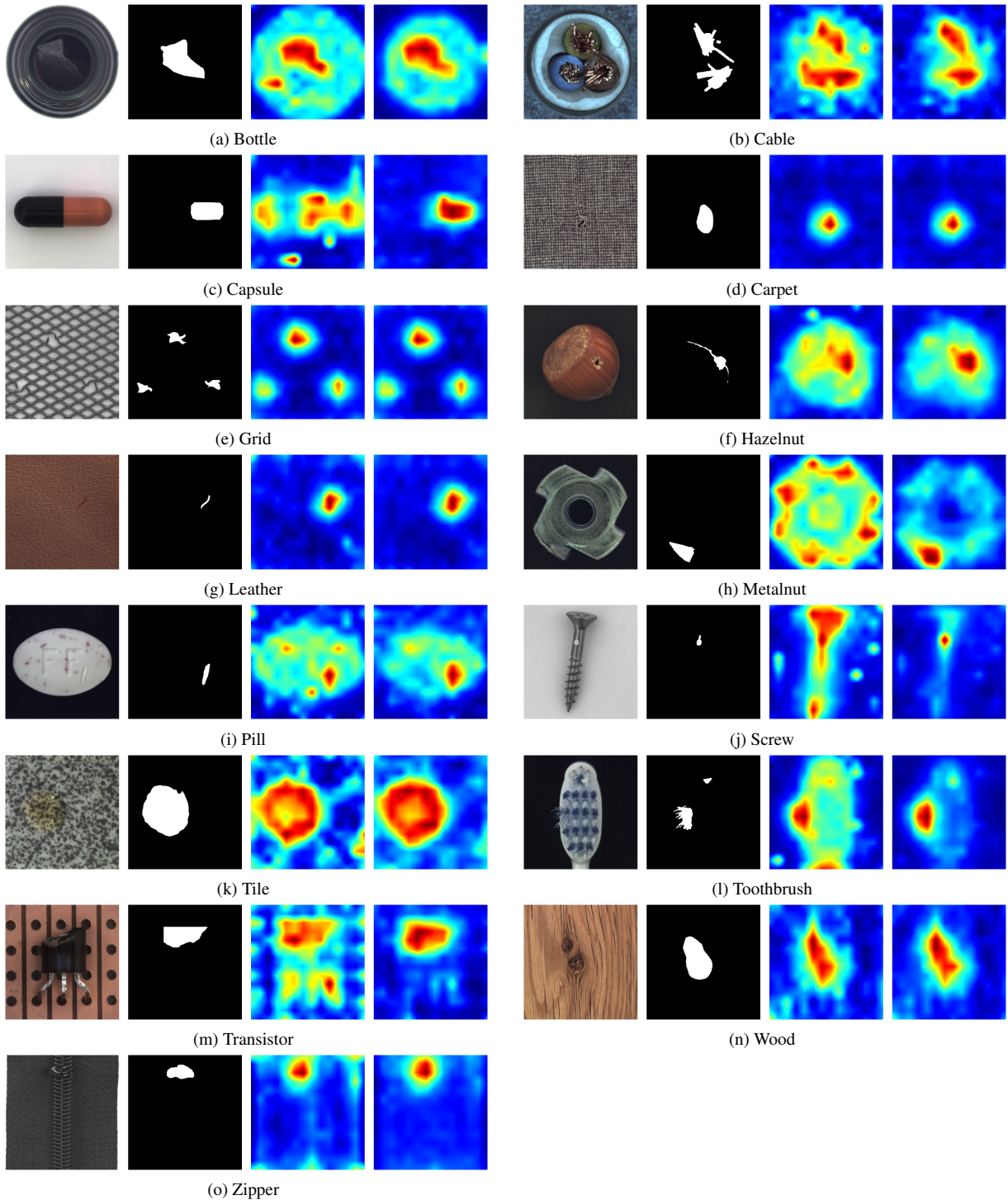


Figure 7. Qualitative Comparison of Anomaly Detection Results Across 15 Categories Using a Baseline Method *UniAD* and *COAD*. Each subfigure shows: (from left to right) the original image, ground truth, result from the baseline method, and the result after applying *COAD*.

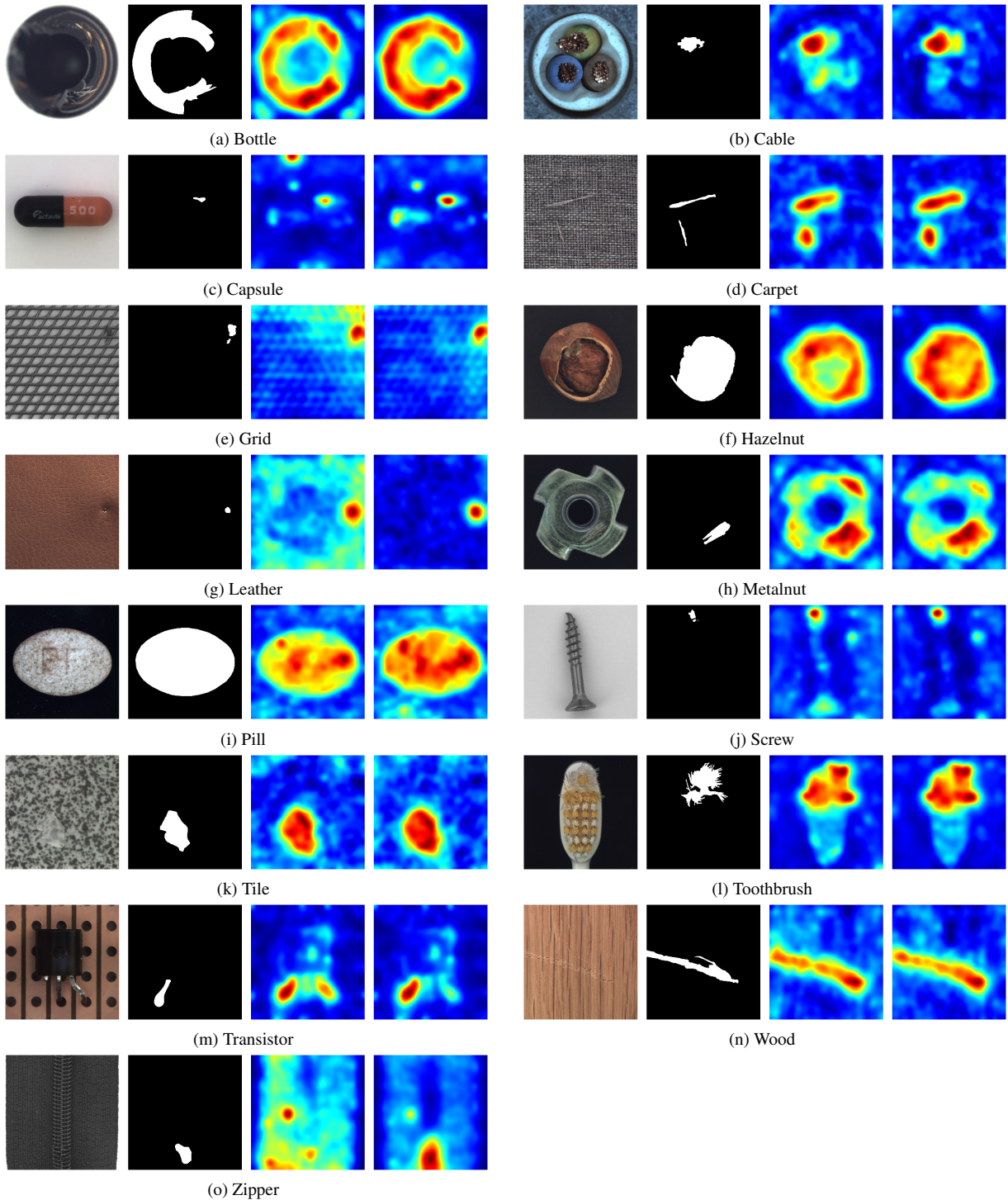


Figure 8. Qualitative Comparison of Anomaly Detection Results Across 15 Categories Using a Baseline Method *DiAD* and *COAD*. Each subfigure shows: (from left to right) the original image, ground truth, result from the baseline method, and the result after applying *COAD*.